

Towards Optimized Charge Transport in Multilayer Reduced Graphene Oxides

Mustafa Neşet Çınar,[†] Aleandro Antidormi,[‡] Viet-Hung Nguyen,[¶]

Alessandro Kovtun,[§] Samuel Lara Avila,^{||} Andrea Liscio,[⊥]

Jean-Christophe Charlier,[¶] Stephan Roche,^{*,‡,#} and Hâldun Sevinçli^{*,†}

[†]*Department of Materials Science and Engineering, Izmir Institute of Technology, 35430 Urla, Izmir, Turkey.*

[‡]*Catalan Institute of Nanoscience and Nanotechnology, CSIC and The Barcelona Institute of Science and Technology, Campus UAB, Bellaterra, 08193 Barcelona (Cerdanyola del Vallès), Spain.*

[¶]*Institute of Condensed Matter and Nanosciences, Université catholique de Louvain (UCLouvain), B-1348 Louvain-la-Neuve, Belgium.*

[§]*Consiglio Nazionale delle Ricerche, Istituto per la Sintesi Organica e la Fotoreattività, (CNR-ISOF), via Gobetti 101, 40129 Bologna, Italy.*

^{||}*Department of Microtechnology and Nanoscience, Chalmers University of Technology, Kemivägen 9, 41296 Gothenburg, Sweden.*

[⊥]*Consiglio Nazionale delle Ricerche, Istituto per la microelettronica e microsistemi, Roma Unit (CNR-IMM), via del fosso del cavaliere 100, 00133 Roma, Italy.*

[#]*ICREA–Institutió Catalana de Recerca i Estudis Avançats, 08010 Barcelona, Spain*

E-mail: stephan.roche@icn2.cat; haldunsevincli@iyte.edu.tr

Abstract

In the context of graphene-based composite applications, a complete understanding of charge conduction in multilayer reduced graphene oxides (rGO) is highly desirable. However, these rGO compounds are characterized by multiple and different sources of disorder depending on the chemical method used for their synthesis. Most importantly the precise role of interlayer interaction in promoting or jeopardizing electronic flow remains unclear. Here, thanks to the development of a multiscale computational approach combining first-principles calculations with large scale transport simulations, the transport scaling laws in multilayer rGO are unraveled, explaining why diffusion worsens with increasing film thickness. In contrast, contacted films are found to exhibit an opposite trend when the mean free path becomes shorter than the channel length, since conduction becomes predominantly driven by interlayer hopping. These predictions are favourably compared with experimental data and open a road towards the optimization of graphene-based composites with improved electrical conduction.

Understanding charge transport in multi-layered van der Waals materials has become an attractive and challenging problem, in the perspective of both fundamental and applied research on graphene-based composites.^{1,2} Indeed, graphene-related materials (including chemically disordered graphene like rGO) have shown remarkable capability to improve charge and thermal conductivities of many insulating flexible materials such as organic polymers, suggesting them as the privileged filler material to reinforce, diversify and improve the properties and performances of traditional materials used in wearables, flexible electronics, conducting textiles and thermoplastics. However, the accurate understanding of the microscopic mechanisms leading to transport in these complex systems is still a matter of debate. Indeed, recent experimental studies³⁻⁵ suggested the key role played by various types of defects, as well as interlayer interaction in the transport mechanisms taking place inside the graphene-based composites.

More specifically, transport characteristics in multilayered rGO⁵ were observed to change from a conventional Efros-Shkloskii variable range hopping (ES-VRH) to a temperature-dependent power-law regime, with increasing the number of stacked layers. Such findings

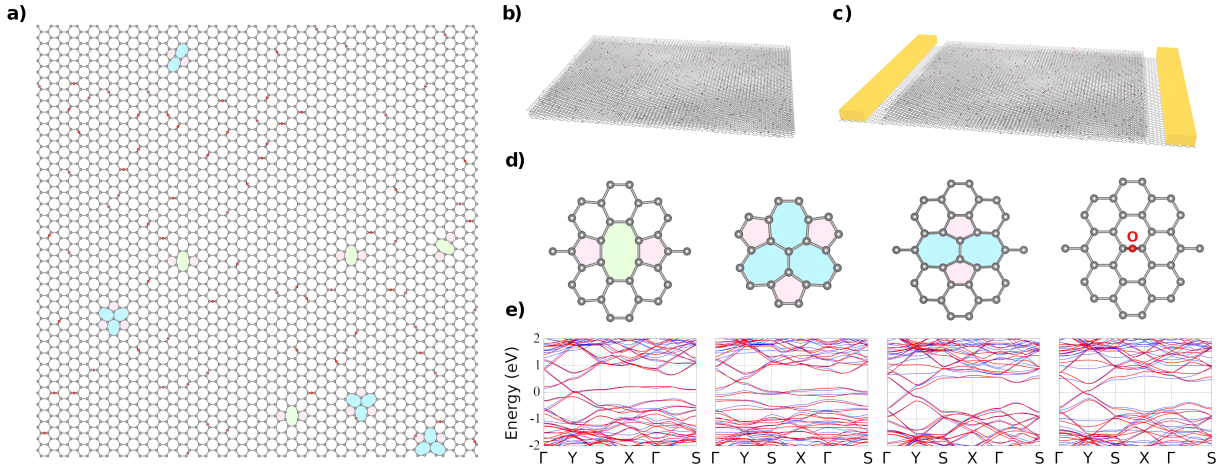


Figure 1: Reduced graphene oxide hosts different types of defects that are randomly distributed (a), where carbon atoms are colored with gray, oxygen with red. Pentagon, heptagon and octagons are indicated with red, blue and green shades. Charge transport calculations in typical multilayered rGO models are investigated in rGO using (b) the Kubo formalism to estimate the bulk electronic conductivity, and (c) the Landauer-Büttiker approach in a conventional device geometry. (d) Atomic structures of various incorporated defect types (pristine divacancy (585), reconstructed divacancy (555-777), Stone-Wales (55-77) and epoxy defects) and their corresponding tight-binding models (e) extracted from *ab initio* band-structure calculations.

do not apparently depend on any length scale of the system, since they are observed in both micrometric networks of few nanosheets partially overlapping, as well as in centimeter-scale thin films built from billions of rGO nanosheets randomly stacked. Besides, the resulting localization length is also found to increase (by three orders of magnitude) with both the aromatic content and the thickness of the thin films as well, while being roughly independent on the lateral size nanosheet. Accordingly, the main contribution to transport properties in multilayered rGO with random stacking likely stems from a bulk contribution, with marginal nanosheet edge effects.⁵

Here, we investigate charge transport in rGO thin films using state-of-the-art modelling techniques and compared the results with experimental measurements. The multilayered rGO models are constructed using a rectangular ribbon-like geometry with a width of 20 nm, and periodic boundary conditions in the transverse direction. Disorder is introduced by incorporating random distributions of chemical defects (Fig. 1a) such as divacancies (0.29%),

Stone-Wales defects (0.01%) and epoxides (4.7%). Such chemical nature and densities of defects have been extracted from atomistic samples of rGO obtained by classical molecular simulations of the thermal reduction process of graphene oxide (GO) sheets.⁶ More specifically, to produce the models, we employ the thermal annealing protocol described in Ref. 6, since it reproduces the main structural features observed in measured rGO samples. In these MD simulations, large-scale GO samples with an initial equivalent concentration of epoxide and hydroxyl groups, amounting to a O/C ratio of 35%, were annealed at 900 °C. At the end of the annealing process, the final concentration of oxygen atoms was found to be approximately 5%, in excellent agreement with the experimental results reported in Ref. 5.

These chemical defects are known to induce lattice distortion and charge redistribution locally around their spatial location.⁷⁻¹² Since these detrimental effects are local, rGO models with defect concentrations similar to those investigated in this study can be modeled using a conventional tight-binding (TB) Hamiltonian (as for graphene) but with specific adjustments made locally around the defect position. Within such a framework, the Hamiltonian of the rGO system presents a simple form allowing to further perform large scale transport calculations in realistic samples containing more than 10^6 atoms and with varying defect concentrations. The parametrized p_z TB Hamiltonian reads

$$H_0 = \sum_{\langle p,q \rangle} \gamma_{pq} c_p^\dagger c_q, \quad (1)$$

where in-plane couplings are limited to nearest neighboring interactions. In contrast with other models in the literature (see Refs. 13,14), the effects of chemical defects are described by adjusting properly the TB parameters to recover *ab initio* results. The optimization of these TB parameters for each specific single defect are obtained by fitting first-principles electronic band structures of graphene supercell containing a single defect (see Supporting Information).

Importantly, the change in C-C bond length due to the lattice distortion around the defects is accounted by computing the hopping energies as a function of C-C bond length (r_{pq}) and defining $\gamma_{pq} = \gamma_0 \exp[-\beta(r_{pq}/r_0 - 1)]$ with nearest-neighbor hopping energy $\gamma_0 = -2.6$ eV, nearest-neighbor distance $r_0 = 1.42$ Å and the decay parameter $\beta = 3.37$.¹⁵ The local doping due to the localized states induced by defects and impurities is also included by modulating onsite energies as a distance-decay function centered at the defect positions. Since the atomic positions are altered around defects, the parametrization for interlayer coupling also requires to account for changes in interatomic distances compared to Bernal graphite (AB-stacking). Consequently to determine TB couplings in presence of varying bond lengths around structural defects, an exponential decay-based model formula is used following $\gamma(r) = \gamma_1 \exp(\beta_z(1 - r/z))$ with interlayer coupling energy $\gamma_1 = 0.36$ eV, the corresponding decay parameter $\beta_z = 24.99$ and interlayer distance $z = 3.34$ Å.^{16,17} Further details and comparison against density functional theory and other methods are given in the Supporting Information. The different types of considered defects used in the model are illustrated in Fig. 1d. The electronic bands obtained from TB parametrization are in excellent agreement with first-principles density functional theory results (Fig. 1e). It is worth mentioning that the concentration of defects is large enough so as to randomize carriers' momenta (more than a hundred scatterings within interlayer diffusion length) and hence the transport properties are not expected to depend on the relative twist angle between layers.

Kubo-Greenwood (KG) and Landauer-Büttiker (LB) transport formalisms are used to study the electronic conductivity and conductance in multilayered rGO models and for varying transport geometries (see Fig. 1b-c, respectively). LB method allows to include the charge injection from contact electrodes (Fig. 1c) whereas the KG method gives access to bulk properties¹⁸ (Fig. 1b). These two techniques enable contrasting bulk properties with “device” related transport (see Supporting Information for details). Note that neither electron-phonon coupling nor many-body effects are included in the present study.

Fig. 2a presents the energy-dependent conductance for the mono-, bi- and trilayer rGO

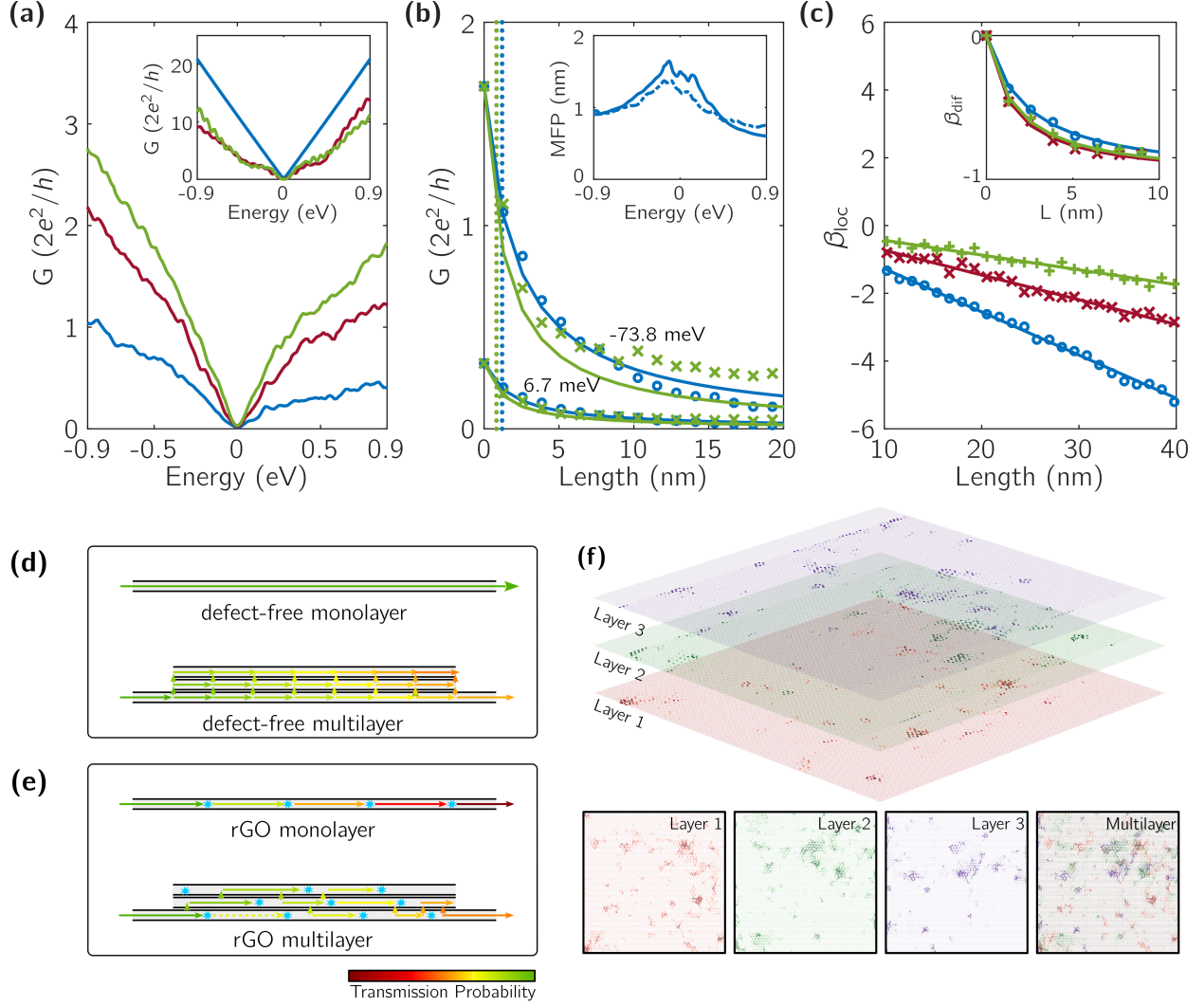


Figure 2: (a) Electronic conductance of mono/bi/tri-layer rGO devices (blue, red, green curves, respectively) as a function of energy. The conductance is found to increase with the number of rGO layers, in contrast with stack of pristine graphene (inset). (b) Electronic conductance of mono- and tri-layered rGO systems for $E = 6.7$ meV (lower region) and $E = -73.8$ meV (upper region) estimated by LB (markers) and Eqn. 2 (solid lines). Mean free paths used in Eqn. 2 are determined by using KG method. Diffusive versus localized regimes in multilayered rGO devices are distinguished by referring to the β -function (c). Transport regimes in pristine and defective stacks are illustrated in (d-e). (f) Local density of states (LDOS) around the Fermi level in multilayer rGO is shown for a relatively smaller sample. LDOS for individual layers and the multilayer are shown in the below panels. Red, green, blue correspond to individual layers from bottom to top.

for identical defect concentration, calculated within the LB approach. When layers are free from defects (pristine graphene), adding new layers will act as supplemental scattering

source, hence reducing the total conductance (see Fig. 2a-inset). Indeed, in defect-free monolayer graphene, transport is ballistic and a maximum V-shaped conductance curve is obtained. When more clean layers are stacked on top of this graphene layer, new scattering channels are opened and an interface resistance is formed. Consequently, the conductance of bi- and tri-layers (multilayered stack) is reduced below the one of pristine monolayer graphene. Actually, such conductance decay is not specific to disorder-free systems but is also observed in low-defect concentrations as well (see Fig. S6). Importantly, this reduction of the electronic transmission is found when the electrodes are attached to the bottom layer and it decreases in a non-monotonic way with the number of added layers. This behavior can be understood as driven by complicated interference processes taking place across the layers and throughout the central region.

In sharp contrast, in strongly disordered rGO systems, the electronic behavior is opposite, in the sense that the higher the number of added layers on the stack, the larger the conductance (Fig. 2a-main frame). This counterintuitive result suggests that the interlayer hopping is opening more conductive channels once the localization length of bottom layer is short enough due to strong in-plane disorder. The two opposite roles played by interlayer coupling in defect-free and defective multilayers are pictured in Fig. 2d-e.

To better understand the electronic transport mechanisms in mono- and multilayered rGO systems, we perform a scaling study of the conductance to better differentiate between diffusive and localized regimes. Figure 2b shows results for the mono- to multilayered rGO systems presenting the same defect density. Clear evidences for different scaling behaviors is observed (note that conductance values from LB simulations are marked with circles (monolayer) and crosses (trilayer)). In the diffusion regime, the conductance dependence with the length is theoretically expected to scale as function of the mean-free-path (ℓ_{mfp}) and the defect-free conductance (G_{Graphene}) of the system (at a given energy) following

$$\frac{1}{G} = \frac{1}{G_{\text{Graphene}}} \left(1 + \frac{2}{\pi} \frac{L}{\ell_{\text{mfp}}} \right), \quad (2)$$

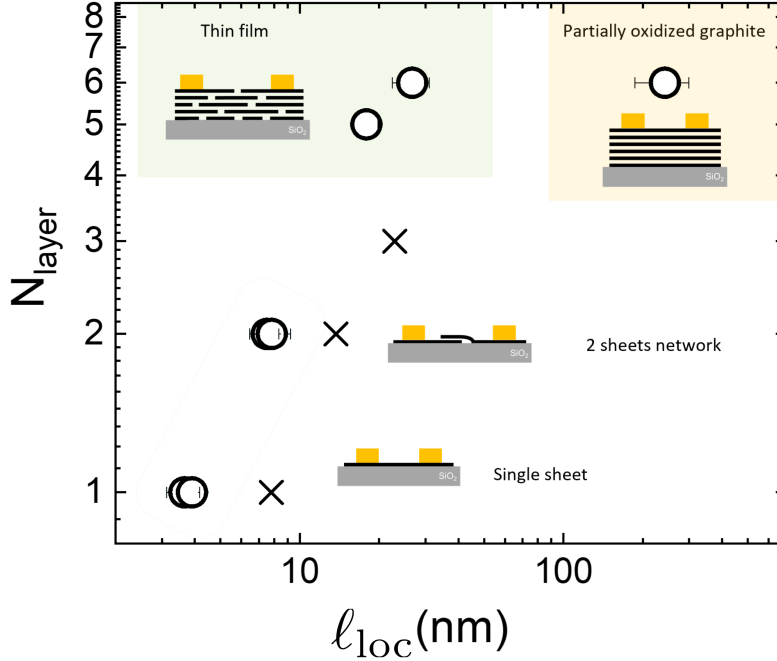


Figure 3: Localization lengths for varying number of layers. Circles represent experimental values, crosses are simulation results. $N_{\text{layer}} \leq 6$ stands for randomly stacked rGO sheets, and the last data point is for partially oxidized graphite. Experimental l_{loc} values are calculated using different dielectric constants. In the case of single or few stacked layers, we estimate $\epsilon_r = 2.5$ from the average of the dielectric constant of the substrate ($\text{SiO}_2 = 3.9$) and vacuum/air ($= 1$),²⁰ while for RGO thin film we assume $\epsilon_r = 3.5$,²¹ and $\epsilon_r = 15$ for partially oxidized graphite.

where L is device length.¹⁹

For short enough channel length the computed conductance scaling is indeed well described by the diffusive formula (Eqn. 2), allowing the extraction of l_{mfp} from simulations. For the chosen disorder features, l_{mfp} in the range of 1-2 nm are obtained (Fig. 2b-inset), regardless the chosen transport formalism. As the number of layers is increased, l_{mfp} decreases slightly (Fig. S5). We note that we here report the scaling behavior of G values for two selected energies (6.7 meV and -73.8 meV) but the trends are similar at all energies around the charge neutrality point (CNP).

We further observe that for channel length $L > 10$ nm, the conductance values for the monolayer are below the diffusion curve (which are plotted by solid lines). This pinpoints the onset of localization effects. However for the trilayer case, a puzzling sudden change of

the conductance behavior is seen for a channel length of 10 nm. To further substantiate this striking difference of the conductance scaling between monolayer and multilayered stack, we investigate the localization regime and capture quantitative information about the localization lengths. LB simulations are performed on rGO systems with long channel lengths and using the scaling function defined as $\beta = \partial \ln G / \partial \ln L$.²² Substituting the corresponding expressions for diffusion and localization, β can be written as $\beta_{dif} = -(1 + \pi \ell_{mfp} / 2L)^{-1}$ in the diffusive regime, whereas $\beta_{loc} = -L / \ell_{loc}$ in the localization regime with ℓ_{loc} being the localization length. Both scaling functions (β_{dif} and β_{loc}) are presented in Fig. 2c versus the device length. The solid curves represent predictions of the above-mentioned analytical formulas, whereas the markers are directly obtained from the simulation (for an energy of 6 meV) without referring to ℓ_{mfp} or ℓ_{loc} , since the scaling functions can be expressed as $\beta_{dif} = G / G_{\text{Graphene}} - 1$ and $\beta_{loc} \propto \ln G$.

On one hand, for the short-channel rGO devices, the diffusive regime is confirmed since the $1/L$ behavior is observed when using ℓ_{mfp} (see Fig. 2c-inset). On the other hand, localization regime is obtained for longer-channel rGO devices, and the evaluated localization lengths varies with the number of layers: 7.8 nm for monolayer, 13.7 nm for bilayer and 22.9 nm for trilayer. Thus, when increasing the number of layers, hopping transport gives rise to larger transmission amplitudes compared to diffusion because of the enhancement of ℓ_{loc} , in very good agreement with the experimental findings as shown in Fig. 3.

Such behavior well agrees with experimental findings achieved on rGO devices with different number of layers (N_{layer}) and similar chemical structure (*i.e.* sp² content $96 \pm 1\%$).⁵ Figure 3 collects the results obtained comparing seven different systems ranging from the single nanosheet ($N_{\text{layer}} = 1$) to a flake of partially oxidized graphite ($N_{\text{layer}} = 6$). Differently, all the other devices ($2 \leq N_{\text{layer}} \leq 6$) are assemblies of rGO sheets randomly stacked. According with the results reported in Ref. 5, all of the six devices reveal ES-VRH transport mechanisms at low temperatures ($10 \text{ K} < T < 100 \text{ K}$). Thus, the corresponding localization length (ℓ_{loc}) is calculated using the temperature-dependent electrical resistivity

curves $\rho(T) = \rho_{0,VRH} \exp\{A\epsilon_r\ell_{loc}T\}^{-1/2}$ where $\rho_{0,VRH}$ is a prefactor for resistivity, ϵ_r is the relative dielectric constant of the material and $A = 2.8e^2/4\pi\epsilon_0k_B = 0.021 \mu\text{m}^{-1}\text{K}^{-1}$ for a 2D system (see Supporting Information for more details). rGO devices have ℓ_{loc} values varying from ca 4 nm to 30 nm, showing the same trend and the same order of magnitude when compared with the simulations. It is noteworthy to underline that in the case of partially oxidized graphite the corresponding ℓ_{loc} value is one order of magnitude larger amounting to 250 nm, clearly evidencing the combined role of the crystalline structure and the dielectric properties. Such aspects are out of the scope of this work and some details related to the experimental setup and the device characterizations are reported in the Supporting Information.

The substantial increase in the localization lengths is thus a key transport feature to distinguish between various multilayered rGO devices and which can be rationalized within the variable range hopping (VRH) framework.²³ Indeed, at zero temperature, the energy separation between two localized states should be very small to enable significant hopping, with probability proportional to $e^{-2\alpha R}$ (with $1/\alpha$ being the attenuation length for the localized states and R being the spatial separation of states). The hopping probability between two states ψ_A and ψ_B , which have similar energies and are localized at the bottom layer well-separated from each other, should thus be strongly enhanced if a third state ψ_C is localized at the upper layer and between ψ_A and ψ_B . Therefore layers with localized states have enhanced transmission when stacked. In Fig. 2f, the local density of states (LDOS) is plotted for a trilayer rGO sample. It is clearly visible that states localized at different layers tend to fill the spatial gaps when they are superimposed. This can qualitatively explain the enhancement of ℓ_{loc} with number of layers.

The interlayer coupling thus plays a crucial role in multilayer transport. In low defect concentrations, it is a source of scatterings which impedes transport, whereas in highly-defective rGO multilayers, it tends to promote longer state delocalization. The contact geometry is also a major factor in transport across the layers. To gain further information

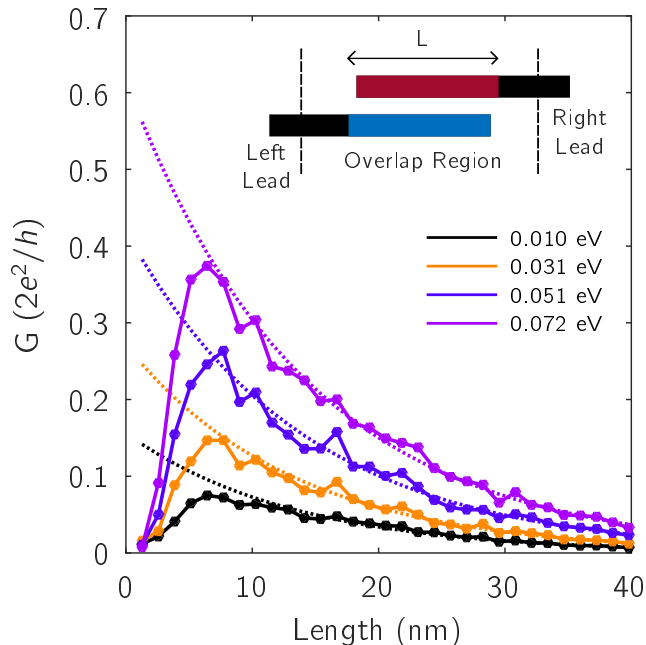


Figure 4: Conductance as a function of overlap length in bilayer reduced graphene oxide when the electrodes are connected to different layers. Dotted curves represent exponential decay.

about the combined roles of interlayer coupling and contact geometry, we simulate a situation where the device is made from overlapping bilayer rGO in which the injection and collection takes place at different layers (inset of Figure 4). We compute the conductance with different overlap distances, L , which is also the length of the central region. As shown in Fig. 4, the conductance rapidly increases with L at short distances because the overlap area enhances the probability for a carrier to diffuse from one layer to the other. Differently, for overlap distances longer than 10 nm, the conductance decays exponentially with L , indicating that the localization behavior prevails over the interlayer diffusion. The maximum conductance is achieved at around 7 nm, which marks the interlayer diffusion length (ℓ_{inter}). We have checked the dependence of ℓ_{inter} in clean structures, and found very similar values, which proves that ℓ_{inter} is dictated by the strength of interlayer coupling and not by the disorder content. We can actually estimate a length scale for interlayer diffusion as $h v_F / \gamma_1 = 11.5$ nm, where the Fermi velocity is $v_F = 10^6$ m/s and the interlayer coupling strength is $\gamma_1 = 0.36$ eV. The

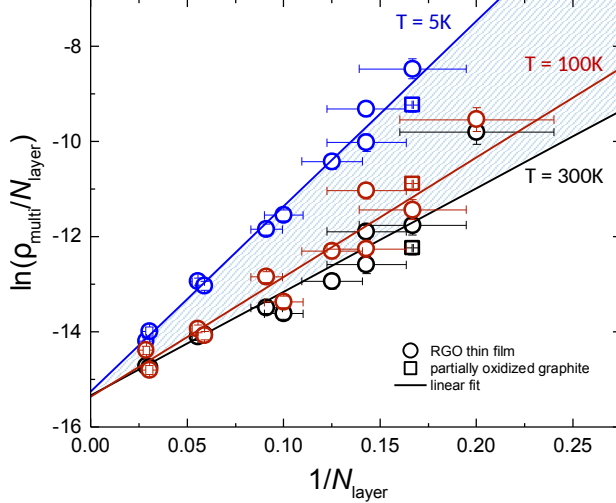


Figure 5: Scaling of multilayer resistivity with the number of layers is plotted as $\ln(\rho_{\text{multi}}/N_{\text{layer}})$ versus $1/N_{\text{layer}}$. Experimental data of multilayer rGO (circles for devices reported in Ref. 5 and square for partially oxidized graphite) acquired at different temperatures show linear dependence, in good agreement with the theoretical prediction for scaling (cf. Eqn. 3). All the linear fitting curves calculated at different temperatures are included between the two curves acquired at 5 K and 300 K (dashed area).

comparison $\ell_{\text{inter}} \gg \ell_{\text{mfp}}$ in the simulated structures is the reason behind the fact that ℓ_{mfp} is weakly affected from the increase in the number of layers. On the other hand, since ℓ_{inter} is comparable with the monolayer localization length, there is room for localized carriers to further spread over the neighboring layers. To clarify the effect of contact geometry on transport, we have considered the electrodes with the same number of layers as in the central region. In this geometry, as expected, the conductance increases with the number of layers both in clean and defective samples, but the behavior of neither ℓ_{mfp} nor ℓ_{loc} are considerably affected.

Finally, based on these findings, the scaling of the resistivity with the number of layers can be expressed quantitatively. In highly defective rGO multilayers ℓ_{mfp} changes only slightly with the number of layers but ℓ_{loc} increases linearly with N_{layer} . Using the fact that ℓ_{loc} is proportional to the number of transmission channels and ℓ_{mfp} ,^{24,25} one can approximate the transmission probability across multilayer rGO in terms of that of the monolayer as

$\mathcal{T}_{\text{multi}} = \mathcal{T}_{\text{mono}}^{1/N_{\text{layer}}}$. Correspondingly the resistivities (ρ) satisfy the following relation,

$$\frac{1}{N_{\text{layer}}} \left(\frac{\rho_{\text{multi}}}{\rho_0} \right) = \left(\frac{\rho_{\text{mono}}}{\rho_0} \right)^{1/N_{\text{layer}}}, \quad (3)$$

where $\rho_0 = hA_{\text{mono}}/2e^2L$ is a system wide constant A_{mono} being the cross section area for a monolayer. Namely, we predict a linear dependence of $\ln(\rho_{\text{multi}}/N_{\text{layer}}) \sim 1/N_{\text{layer}}$ for film thickness larger than the mean free path. For the sake of comparison, we analyze a data set of 11 rGO devices with similar chemical structure (i.e. sp^2 content = $96 \pm 1\%$) and film thickness ranging from 2 nm to 13 nm, i.e. $5 < N_{\text{layer}} < 35$. Note that, we do not need to assume any values for A_{mono} and ρ_0 or measure them, but they are used in order to relate resistivity and conductance so as to compare experimentally measured values with simulated ones through the scaling relation (Eqn. 3).

Figure 5 shows the correlation plot $\ln(\rho_{\text{multi}}/N_{\text{layer}})$ vs $1/N_{\text{layer}}$ for each device displaying the resistivity values acquired at different temperatures: 5 K, 100 K and 300 K, the lowest, an intermediate and the highest measured, respectively. A total of datasets corresponding to 43 different temperatures were analyzed and the remaining 40 curves – not depicted in the figure – are included between the two curves acquired at 5 K and 300 K (dashed area). In all the cases we observe a linear trend: $y = m \cdot x + q$ in excellent agreement with Equation (3). Moreover, we obtain that the slope $m = \ln(\rho_{\text{mono}}/\rho_0)$ decreases with increasing temperature, while the y -intercept (q) is a constant value corresponding to $\rho_0 = \exp(q) = (2.1 \pm 0.2) \times 10^{-7} \Omega \cdot \text{m}$. Similarly, a linear behavior is achieved in the case of rGO devices with lower amount of the aromatic content (77% and 86%, see Fig, S9) where the resistivity values increase with the oxidation degree, as expected. Summarizing the experimental findings, ρ_{mono} is the single-layer resistivity (temperature-dependent) while ρ_0 does not depend on the temperature, being therefore a kind of resistivity scaling factor only depending on the aromatic content of the device.

Conclusion

We have reported quantum simulations on realistic models of multi-layered rGO which reveal the complex interplay between disorder and interlayer interactions in dictating the dominant transport mechanism. Depending on the concentration of defects, multilayer interaction can enhance or suppress the system conductance, which results from the competition between the mean free path ℓ_{mfp} and the interlayer diffusion length ℓ_{inter} . When about 5% of the carbon atoms are involved in defected regions, ℓ_{inter} becomes much longer than ℓ_{mfp} . In that case, intralayer scattering largely dominates over interlayer diffusion, leading to a weak dependence of ℓ_{mfp} on N_{layer} .

On the other hand, $\ell_{\text{loc}} \sim \ell_{\text{inter}}$, so that a localized state in one of the layers has enough extension for tunneling to an adjacent one. If ℓ_{inter} was much larger than ℓ_{loc} , the tunneling rates would be much smaller. Once $\ell_{\text{inter}} \sim \ell_{\text{loc}}$, tunneling rates are appreciable and charge delocalization is promoted. While ℓ_{mfp} is weakly dependent on N_{layer} , ℓ_{loc} increases with N_{layer} as expected from a generalization of the Thouless relationship for one-dimensional conductors. This unprecedented interplay between transport length scales is a specific result of 2D layered nature of the multilayer rGO systems. Such mechanism enables hopping transport to overcome the diffusion limit, which is usually the upper bound in bulk systems. Our theoretical analysis enables us to derive a novel scaling rule, which is in perfect agreement with experimental data at various temperature, and consistent with the Thouless relationship. The fundamental findings of this study are not limited to multilayered reduced graphene oxide but could find applications in other two-dimensional stacks as well.

Acknowledgements. The authors acknowledge support from the Flag-Era JTC 2017 project ‘Modelling Charge and Heat trANsport in 2D-materIals based Composites– MECHANIC’. MNÇ and HS acknowledge support from TÜBİTAK (117F480). AA and SR are supported by - MECHANIC reference number: PCI2018-093120 funded by Ministerio de Ciencia, Innovacion y Universidades and the European Union Horizon 2020 research and

innovation programme under Grant Agreement No. 881603 (Graphene Flagship). ICN2 is funded by the CERCA Programme/ Generalitat de Catalunya, and is supported by the Severo Ochoa program from Spanish MINECO (Grant No. SEV-2017-0706). V.-H.N. and J.-C.C. acknowledge financial support from the Fédération Wallonie-Bruxelles through the ARC on 3D nano-architecturing of 2D crystals (N°16/21-077), from the European Union's Horizon 2020 Research Project and Innovation Program — Graphene Flagship Core3 (N°881603), and from the Belgium FNRS through the research project (N°T.0051.18). Computational resources have been provided by the CISM supercomputing facilities of UCLouvain and the CECI consortium funded by F.R.S. -FNRS of Belgium (N°2.5020.11). Authors are particularly grateful to Prof. Paolo Samorì and Marco Gobbi for the scientific assistance to prepare the devices, Valentina Mussi for some supporting measurements and for enlightening discussions.

References

- (1) C. Ferrari, A. et al. Science and technology roadmap for graphene, related two-dimensional crystals, and hybrid systems. *Nanoscale* **2015**, *7*, 4598–4810, Publisher: Royal Society of Chemistry.
- (2) Mohan, V. B.; Lau, K.-t.; Hui, D.; Bhattacharyya, D. Graphene-based materials and their composites: A review on production, applications and product limitations. *Composites Part B: Engineering* **2018**, *142*, 200–220.
- (3) Turchanin, A.; Weber, D.; Büenefeld, M.; Kisielowski, C.; Fistul, M. V.; Efetov, K. B.; Weimann, T.; Stosch, R.; Mayer, J.; Gölzhäuser, A. Conversion of Self-Assembled Monolayers into Nanocrystalline Graphene: Structure and Electric Transport. *ACS Nano* **2011**, *5*, 3896–3904, Publisher: American Chemical Society.
- (4) Silverstein, K. W.; Halbig, C. E.; Mehta, J. S.; Sharma, A.; Eigler, S.; Mativetsky, J. M. Voltage-reduced low-defect graphene oxide: a high conductivity, near-zero temperature coefficient of resistance material. *Nanoscale* **2019**, *11*, 3112–3116, Publisher: The Royal Society of Chemistry.
- (5) Kovtun, A.; Candini, A.; Vianelli, A.; Boschi, A.; Dell’Elce, S.; Gobbi, M.; Kim, K. H.; Lara Avila, S.; Samorì, P.; Affronte, M.; Liscio, A.; Palermo, V. Multiscale Charge Transport in van der Waals Thin Films: Reduced Graphene Oxide as a Case Study. *ACS Nano* **2021**, *15*, 2654–2667, Publisher: American Chemical Society.
- (6) Antidormi, A.; Roche, S.; Colombo, L. Impact of Oxidation Morphology on Reduced Graphene Oxides upon Thermal Annealing. *J. Phys.: Mat.* **2019**, *3*, 015011.
- (7) Cresti, A.; Nemeč, N.; Biel, B.; Niebler, G.; Triozon, F.; Cuniberti, G.; Roche, S. Charge transport in disordered graphene-based low dimensional materials. *Nano Research* **2008**, *1*, 361–394.

- (8) Zhang, Y.; Brar, V. W.; Girit, C.; Zettl, A.; Crommie, M. F. Origin of spatial charge inhomogeneity in graphene. *Nature Physics* **2009**, *5*, 722–726, Number: 10 Publisher: Nature Publishing Group.
- (9) Wang, S.; Wang, R.; Wang, X.; Zhang, D.; Qiu, X. Nanoscale charge distribution and energy band modification in defect-patterned graphene. *Nanoscale* **2012**, *4*, 2651–2657, Publisher: Royal Society of Chemistry.
- (10) Ma, C.; Sun, H.; Zhao, Y.; Li, B.; Li, Q.; Zhao, A.; Wang, X.; Luo, Y.; Yang, J.; Wang, B.; Hou, J. G. Evidence of van Hove Singularities in Ordered Grain Boundaries of Graphene. *Phys. Rev. Lett.* **2014**, *112*, 226802.
- (11) Gao, Y.; Qin, C.; Qiao, Z.; Wang, B.; Li, W.; Zhang, G.; Chen, R.; Xiao, L.; Jia, S. Observing and tuning the density distribution of localized states of monolayer graphene oxide by using external electric field. *Applied Physics Letters* **2015**, *106*, 131103, Publisher: American Institute of Physics.
- (12) Zhang, W.; Lu, W.-C.; Zhang, H.-X.; Ho, K. M.; Wang, C. Z. Lattice distortion and electron charge redistribution induced by defects in graphene. *Carbon* **2016**, *110*, 330–335.
- (13) Leconte, N.; Moser, J.; Ordejón, P.; Tao, H.; Lherbier, A.; Bachtold, A.; Alsina, F.; Sotomayor Torres, C. M.; Charlier, J.-C.; Roche, S. Damaging Graphene with Ozone Treatment: A Chemically Tunable Metal-Insulator Transition. *ACS Nano* **2010**, *4*, 4033–4038.
- (14) Lherbier, A.; Dubois, S. M.-M.; Declerck, X.; Niquet, Y.-M.; Roche, S.; Charlier, J.-C. Transport properties of graphene containing structural defects. *Phys. Rev. B* **2012**, *86*, 075402.
- (15) Pereira, V. M.; Castro Neto, A. H.; Peres, N. M. R. Tight-binding approach to uniaxial strain in graphene. *Phys. Rev. B* **2009**, *80*, 045401.

- (16) Suárez Morell, E.; Correa, J. D.; Vargas, P.; Pacheco, M.; Barticevic, Z. Flat bands in slightly twisted bilayer graphene: Tight-binding calculations. *Phys. Rev. B* **2010**, *82*, 121407.
- (17) Reich, S.; Maultzsch, J.; Thomsen, C.; Ordejón, P. Tight-binding description of graphene. *Phys. Rev. B* **2002**, *66*, 035412.
- (18) Fan, Z.; Garcia, J. H.; Cummings, A. W.; Barrios-Vargas, J. E.; Panhans, M.; Harju, A.; Ortmann, F.; Roche, S. Linear scaling quantum transport methodologies. *Physics Reports* **2021**, *903*, 1–69.
- (19) Datta, S. *Electronic Transport in Mesoscopic Systems*; Cambridge Studies in Semiconductor Physics and Microelectronic Engineering; Cambridge University Press, 1995.
- (20) Jang, C.; Adam, S.; Chen, J.-H.; Williams, E. D.; Das Sarma, S.; Fuhrer, M. S. Tuning the Effective Fine Structure Constant in Graphene: Opposing Effects of Dielectric Screening on Short- and Long-Range Potential Scattering. *Phys. Rev. Lett.* **2008**, *101*, 146805.
- (21) Jung, I.; Vaupel, M.; Pelton, M.; Piner, R.; Dikin, D. A.; Stankovich, S.; An, J.; Ruoff, R. S. Characterization of Thermally Reduced Graphene Oxide by Imaging Ellipsometry. *The Journal of Physical Chemistry C* **2008**, *112*, 8499–8506.
- (22) Abrahams, E.; Anderson, P. W.; Licciardello, D. C.; Ramakrishnan, T. V. Scaling Theory of Localization: Absence of Quantum Diffusion in Two Dimensions. *Physical Review Letters* **1979**, *42*, 673–676.
- (23) Mott, N. F. Conduction in non-crystalline materials: III. Localized states in a pseudogap and near extremities of conduction and valence bands. *Philosophical Magazine* **1969**, *19*, 835–852.

- (24) Thouless, D. J. Localization distance and mean free path in one-dimensional disordered systems. *Journal of Physics C: Solid State Physics* **1973**, *6*, L49–L51.
- (25) Leconte, N.; Lherbier, A.; Varchon, F.; Ordejon, P.; Roche, S.; Charlier, J.-C. Quantum transport in chemically modified two-dimensional graphene: From minimal conductivity to Anderson localization. *Phys. Rev. B* **2011**, *84*, 235420.
- (26) Ryndyk, D. *Theory of Quantum Transport at Nanoscale: An Introduction*; Springer, 2015.
- (27) Sevinçli, H.; Sevik, C.; Çağın, T.; Cuniberti, G. A bottom-up route to enhance thermoelectric figures of merit in graphene nanoribbons. *Scientific Reports* **2013**, *3*, 1632.
- (28) Trambly de Laissardiere, G.; Mayou, D.; Magaud, L. Localization of Dirac Electrons in Rotated Graphene Bilayers. *Nano Letters* **2010**, *10*, 804–808.
- (29) Datta, S. Nanoscale device modeling: the Green’s function method. *Superlattices and Microstructures* **2000**, *28*, 253–278.
- (30) Cheah, C. Y.; Gómez-Navarro, C.; Jaurigue, L. C.; Kaiser, A. B. Conductance of partially disordered graphene: crossover from temperature-dependent to field-dependent variable-range hopping. *Journal of Physics: Condensed Matter* **2013**, *25*, 465303.
- (31) Mott, N. F. On the transition to metallic conduction in semiconductors. *Canadian Journal of Physics* **1956**, *34*, 1356–1368.
- (32) Efros, A. L.; Shklovskii, B. I. Coulomb gap and low temperature conductivity of disordered systems. *Journal of Physics C: Solid State Physics* **1975**, *8*, L49–L51.

Supporting Information

Towards Optimized Charge Transport in Multilayer Reduced Graphene Oxides

Mustafa Neşet Çınar, Aleandro Antidormi, Viet-Hung Nguyen,
Alessandro Kovtun, Samuel Lara Avila, Andrea Liscio, Jean-Christophe Charlier,
Stephan Roche, Hâldun Sevinçli

E-mail: stephan.roche@icn2.cat; haldunsevincli@iyte.edu.tr

Kubo-Greenwood and Landauer-Büttiker methods

An efficient linear scaling approach¹⁸ is used in Kubo transport to estimate the energy- and time-dependent mean squared displacement of the wave-packet that spreads into the investigated atomic structure,

$$\Delta X^2(E, t) = \frac{\text{Tr}[\delta(E - \hat{H})|\hat{X}(t) - \hat{X}(0)|^2]}{g(E)}, \quad (\text{S1})$$

where $g(E) = \text{Tr}[\delta(E - \hat{H})]$ is the density at energy E . The time-dependent semiclassical diffusion coefficient $D(E, t) = \frac{\partial}{\partial t}\Delta X^2(E, t)$ and its asymptotic limit $\tilde{D}(E)$ can then be calculated, allowing for the computation of both the electron conductivity and the mean free path as $\sigma(E) = e^2 g(E)\tilde{D}(E)$ and $\ell_{\text{mfp}}(E) = 2\tilde{D}(E)/v_F(E)$, respectively (with $v_F(E)$ being the carrier velocity). The conductivity values in rGO systems have been averaged over 10 different randomly chosen initial wave packets, and the calculation of the mean-square displacement was carried out through an efficient decomposition in terms of Chebyshev polynomials, with 5000 moments. Note that periodic boundary conditions are employed in

both longitudinal and transverse directions.

Concerning the transport simulations performed using the Landauer-Büttiker technique, the rGO system is partitioned into three regions, namely the left and right electrodes (leads) and the central region. The leads are modeled as scattering free regions made up of the same ideal material. The Green function for the central region is calculated as $\mathcal{G}(E) = [(E + i0^+)I - H_C - \Sigma]^{-1}$, where I is identity matrix, H_C is the Hamiltonian matrix for the central region, and the self-energy term includes effects of the left and right reservoirs as $\Sigma = \Sigma_L + \Sigma_R$. In this work, systems containing as many as 10^6 atoms have been simulated, for which efficient decimation algorithms are implemented.^{26,27} The transmission amplitude is obtained from $\mathcal{T}(E) = \text{Tr} [\Gamma_L \mathcal{G} \Gamma_R \mathcal{G}^\dagger]$, where $\Gamma_{L(R)} = i[\Sigma_{L(R)} - \Sigma_{L(R)}^\dagger]$ are the left (right) broadening matrices. Conductance values are calculated using the Landauer formula,

$$G = \frac{2e^2}{h} \int \left(-\frac{\partial f_{FD}(E, \mu, T)}{\partial E} \right) \mathcal{T}(E) dE, \quad (\text{S2})$$

where e is electron charge, f_{FD} is Fermi-Dirac distribution function, T is temperature (here with 100 K) and $\mathcal{T}(E)$ is the transmission probability for a given energy E . Since low-energy properties are only of interest, transmission coefficients are integrated over 40 k -points in the transverse direction in order to reach sufficiently accurate energy resolution. At last, a geometric average on the transmission function over an ensemble of 20 samples is applied to overcome the sample size effects.

Supplementary details on simulated structures

The types and amounts of defects are deduced from MD simulations replicating the thermal annealing of GO on a computer. In particular, following the protocol in Ref. 6, several atomistic samples of GO have been generated with a total number of atoms as large as 10000 and an initial oxygen concentration of 35%. The thermal reduction of the systems has been simulated for different annealing temperatures and a statistical analysis of the chemical and morphological properties of the resulting rGO samples has been performed. In the table below, a summary of the values of the most relevant chemical species observed in the the samples after reduction is given. At the annealing temperature of 900oC, a final concentration of oxidizing agents of 5% has been found, in extremely good agreement with the experimental samples. From a detailed exploration of the atomistic structures, the concentration and type of defects has been derived and used to model rGO samples for transport calculations.

Table 1: Concentration of different chemical species observed in the atomistic samples of rGO after the reduction process at different annealing temperatures.

	C sp ² (%)	C sp ³ (%)	C-OH (%)	C-O-C (%)	C=O (%)	O-C=O (%)	O/CFIT
GO	32.9	11.5	3.0	43	6.5	3.0	0.35 (imposed)
rGO 300 °C	75.4	10.5	2.9	3.9	4.8	2.5	0.154
rGO 600 °C	83.5	8.8	1.1	3.7	1.1	1.8	0.11
rGO 900 °C	94.1	3.6	0.3	0.8	0.6	0.6	0.05

Supplementary details regarding tight-binding parameters

As explained in the main text, while the change in C-C bond length is modeled by the distance dependence of hopping energies, the local doping due to the localized states induced by defects and impurities are included by adding on-site energies to C-atoms surrounding their position. These on-site energies have the following common form

- ε_D applied to C atoms directly connected to impurities/defects
- ε_n applied to other surrounding C atoms

$$\varepsilon_n = \frac{\varepsilon_0}{1 + (d_n/\lambda_D)^\kappa} \quad (\text{S3})$$

where d_n is the distance from the n^{th} C atom to the considered impurity, ε_0 is the maximum value of ε_n , λ_D is the decay length and the number κ is determined depending on the defect/impurity types.

Oxygen impurity	$\lambda_D = 1.0 \text{ \AA}$	$\kappa = 3$	$\varepsilon_0 = 1.6 \text{ eV}$	$\varepsilon_D = -28.0 \text{ eV}$	
OH group	$\lambda_D = 1.0 \text{ \AA}$	$\kappa = 3$	$\varepsilon_0 = 1.8 \text{ eV}$	$\varepsilon_D = -28.0 \text{ eV}$	
585 defect	$\lambda_D = 5.0 \text{ \AA}$	$\kappa = 5$	$\varepsilon_0 = 1.0 \text{ eV}$	$\varepsilon_D = -1.3 \text{ eV}$	
Stone-Waled defect	$\lambda_D = 1.6 \text{ \AA}$	$\kappa = 5$	$\varepsilon_0 = -1.5 \text{ eV}$	$\varepsilon_D = -1.2 \text{ eV}$	
555-777 defect	$\lambda_D = 8.0 \text{ \AA}$	$\kappa = 5$	$\varepsilon_0 = 0.4 \text{ eV}$	$\varepsilon_{D1} = -1.8 \text{ eV}$	$\varepsilon_{D2} = -0.5 \text{ eV}$

The electronic band structures obtained using the proposed tight binding Hamiltonians are presented in Figs. S2 and S3. Indeed, our proposed tight-binding models reproduce well the low energy bands, compared to the DFT results.

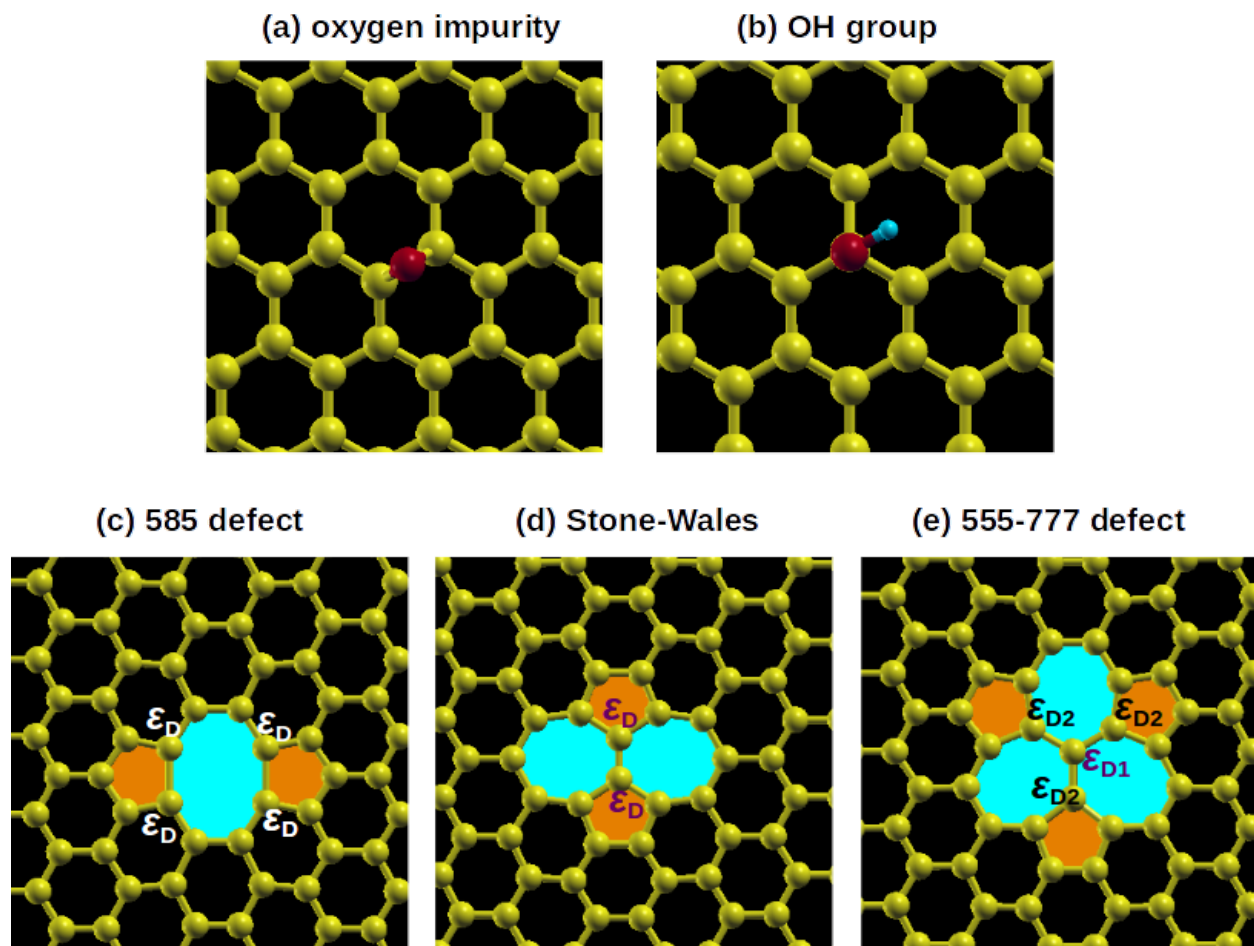


Figure S1: Defects and impurities investigated in this work.

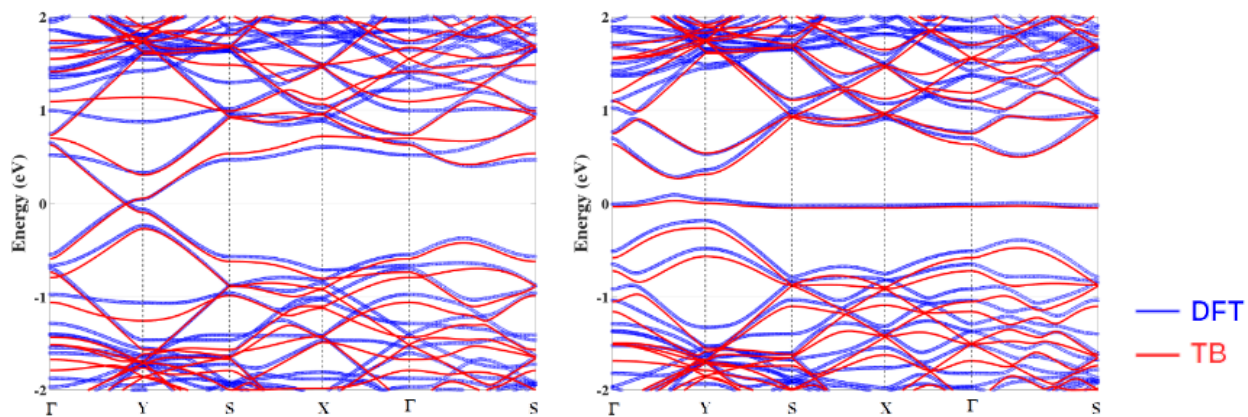


Figure S2: The electronic band structure of graphene with oxygen impurity (left) and OH group (right). TB calculations fit to the DFT results.

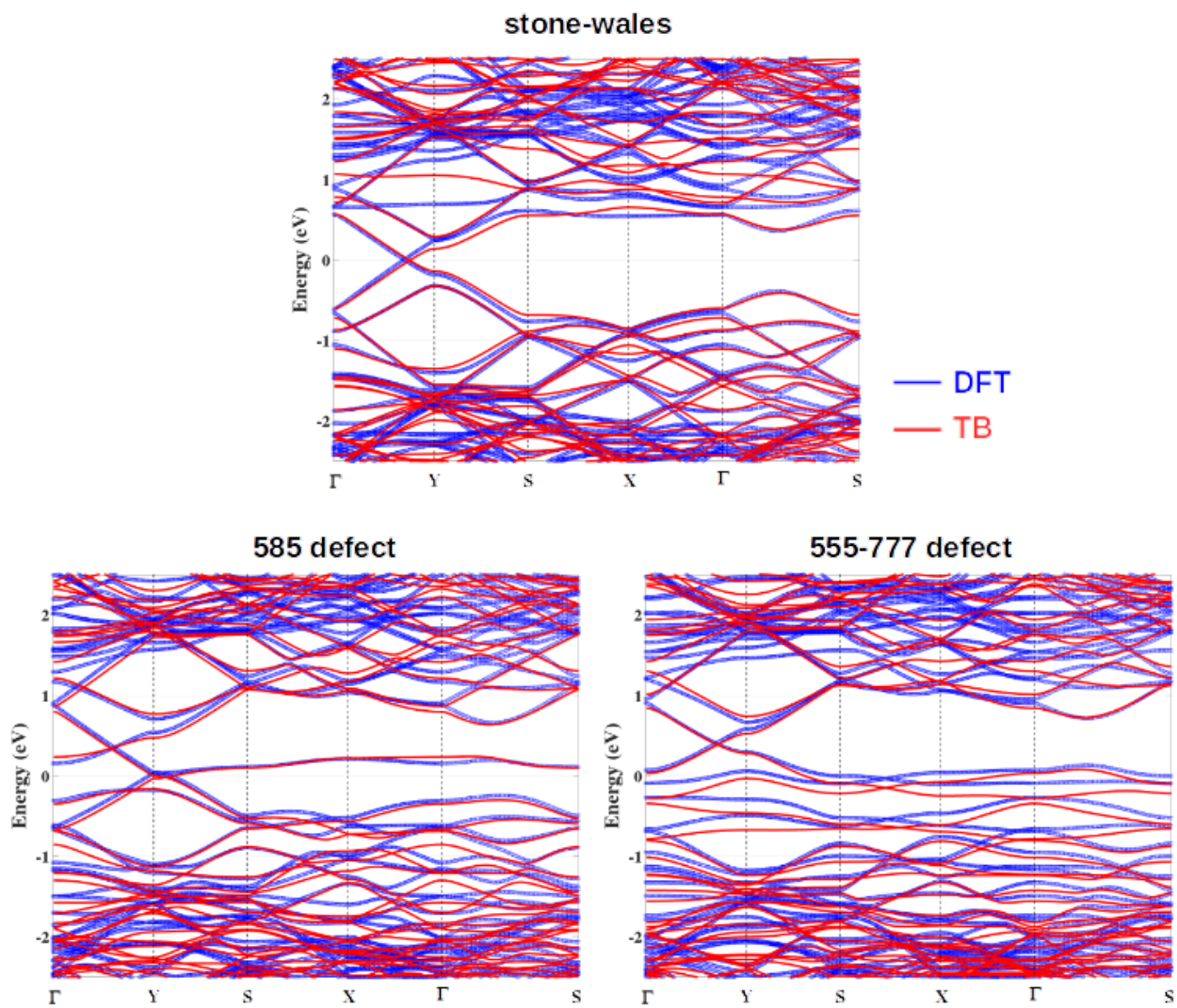


Figure S3: The electronic bandstructure of graphene with structural defects. TB calculations fit to the DFT results.

Other sophisticated models (i.e., larger distance neighbor as well as Slater-Koster like models) generally present a disadvantage that a large number of adjusted parameters are required to model accurately the considered defective systems. This disadvantage also gives rise to some difficulties for the implementation of transport calculations in the large scale devices while the accuracy is not significantly improved. In Fig. S4 a comparison of the computed electronic band structures of bilayer graphene obtained using our used model and Slater-Koster like models in Ref. 28 that has been shown to compute well the electronic structure of both Bernal stacking and twisted bilayer graphene systems.

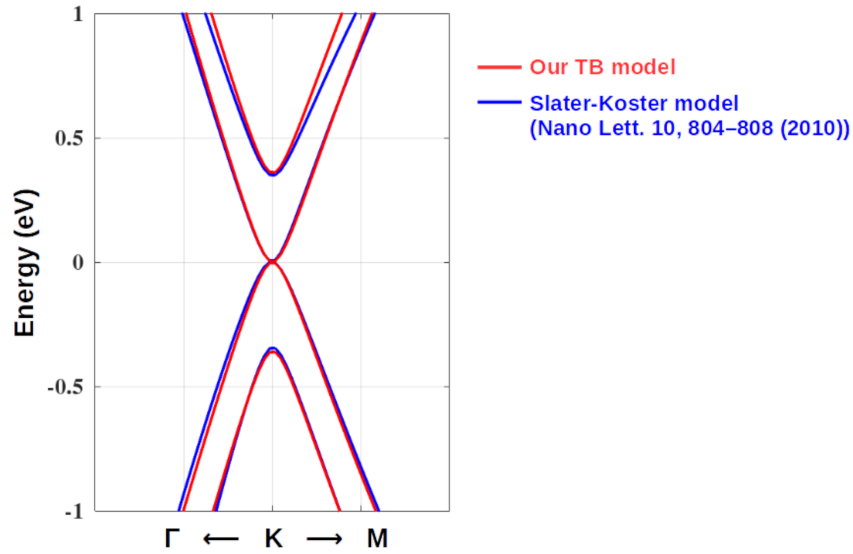


Figure S4: Comparison of the electronic bands of bilayer graphene obtained using our TB Hamiltonian and Slater-Koster like models in Nano Lett. 10, 804–808 (2010).

Note on parametrization and system setups

The tight-binding parametrization for structural defects involves modifying onsite energies of sp^2 orbitals by a value which decays exponentially with the distance, and onsite energies due to defects surrounding a particular atom are taken additive. For Landauer-Büttiker calculations, we also introduced defect-free buffers of 2.57 nm in length between the scattering region and the leads to saturate the effects due to the onsite energies (see Fig.1 right panel), and cutoff radius of 2.57 nm was used as the range of the modification. For the scaling analysis, the central transport channel is lengthened by adding 1.284 nm-length blocks (which corresponds to a mesh resolution of the same length).

Supplementary mean-free-path plots

Mean-free-paths as obtained from Landauer-Büttiker and Kubo-Greenwood simulations with changing layer thickness are shown for comparison in Figure S5. The agreement between two methodologies is remarkable.

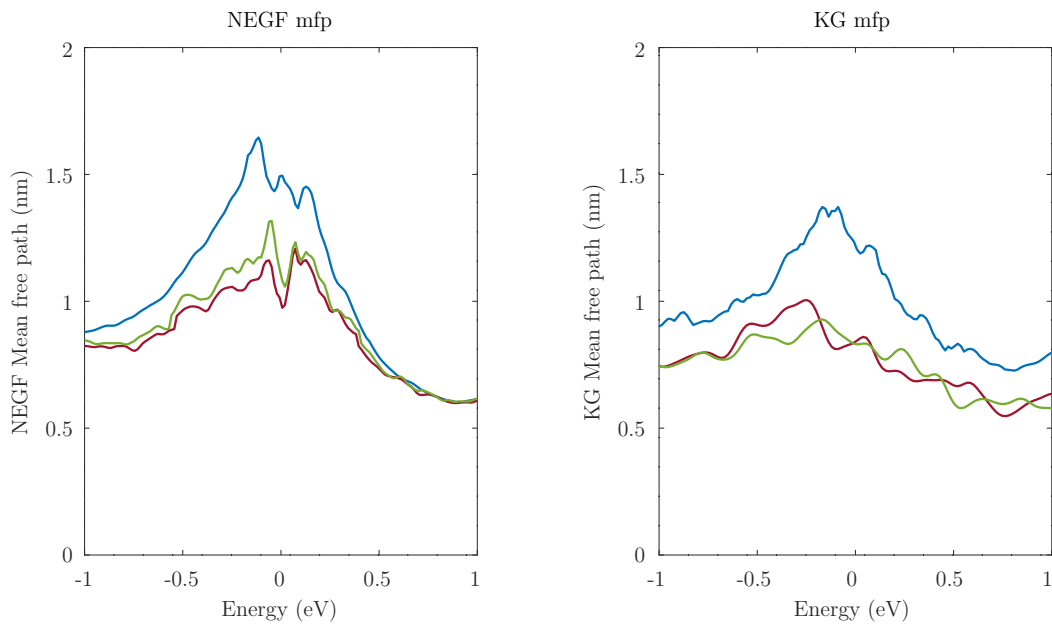


Figure S5: Mean-free-paths for different numbers of layers as obtained from NEGF and KG simulations are shown. Blue, red and green curves represent mono/bi/tri-layer rGO systems.

Supplementary results with lower defect concentrations

We have shown in the main text that interlayer coupling affects charge transport of defect-free and defective systems in opposite ways. Namely, in defect-free systems conductance is reduced with the number of layers, whereas it is enhanced in rGO, which contains 95% sp^2 carbon. Reducing the amount of impurities, it is possible to observe the transition. In Fig. S6, defect concentration is 10 times lower than those in the main text (99.5% sp^2 carbon), where monolayer is observed to have the highest transmission values around the charge neutrality point.

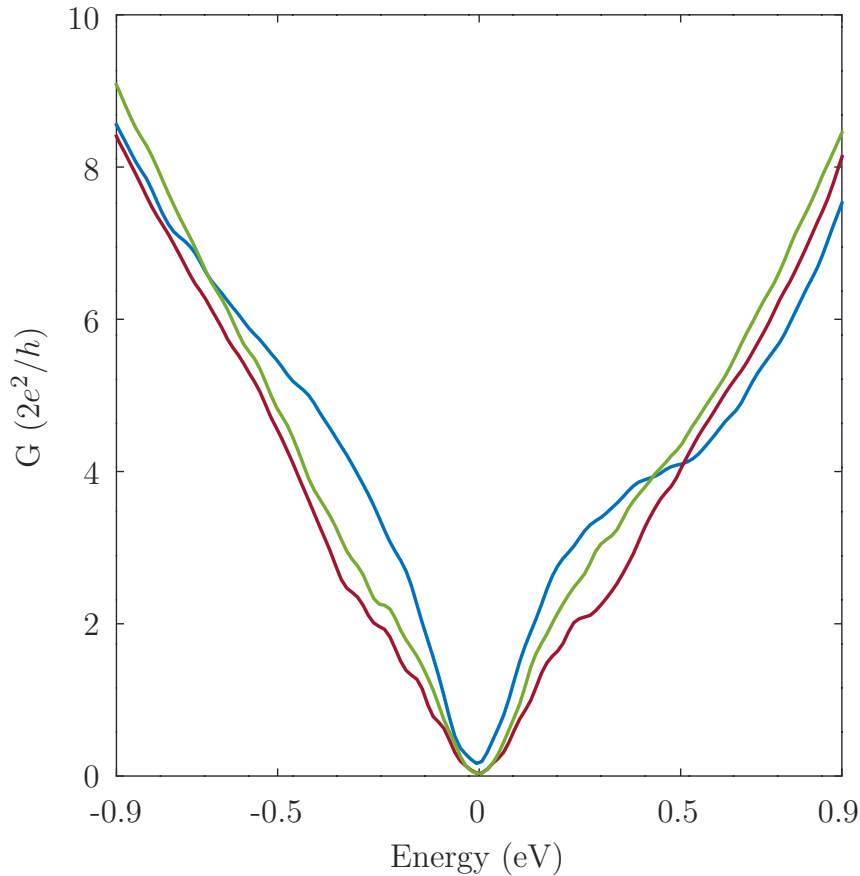


Figure S6: Transmission spectrum through rGO with low concentration of imperfections. The device sizes are the same with those in the main text, impurity concentration is 10 times lower with 99.5% sp^2 ratio. Blue, red and green curves correspond to mono/bi/trilayer rGO, respectively.

Supplementary LDOS plots

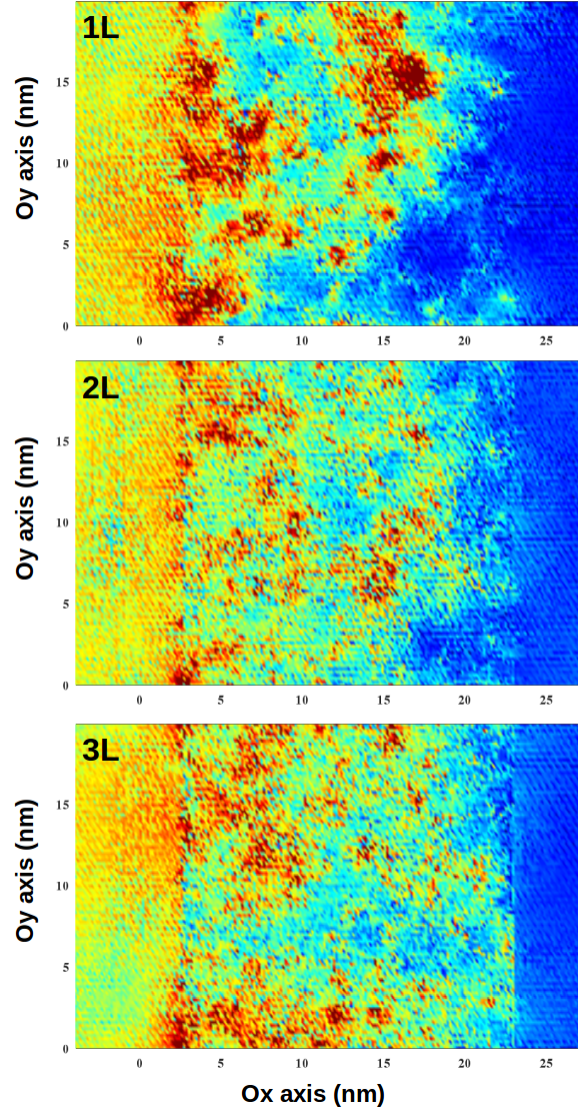


Figure S7: Left injected LDOS plots for mono/bi/tri-layer rGO. High and low LODS values are distinguished on the left/right electrodes. Localization is more pronounced in monolayer, whereas the carrier density more dispersed in trilayer sample.

Using the Green's function method, we could compute the left (right, respectively) injected LDOS,²⁹ reflecting the propagation of electrons from left to right (right to left, respectively) electrodes. In particular, the left-injected LDOS is given by

$$LDOS_L = \frac{G\Gamma_L G^\dagger}{2\pi}. \quad (\text{S4})$$

LDOS in the multilayer zones are averaged over the layers to show the contributions from all layers. The decay of the presented left-injected LDOS along the Ox axis in Fig.S6 is essentially due to scatterings with defects/impurities, manifesting as the electronic localization in the device region. In the monolayer case, charge localization is more pronounced than bilayer and trilayer systems, in agreement with Fig. 2f. Importantly, it is shown that the improved propagation of electrons from left to right electrodes is obtained when increasing number of graphene layers, thus illustrating the transport properties discussed in the main text.

Temperature-dependence of electrical resistivity $\rho(T)$, Efros-Shklovskii variable range hopping model

At low temperature, charge transport in graphene-based materials is typically occurring via charge hopping in a disorder-broadened density of states near the Fermi level $g(E_F)$.³⁰ In the Ohmic regime, the resistivity is typically modelled by a stretched exponential behavior:

$$\rho(T) = \rho_{0,VRH} \exp\left(\frac{T_0}{T}\right)^\beta, \quad (\text{S5})$$

where $\rho_{0,VRH}$ is a prefactor and β is a characteristic exponent. T_0 represents a characteristic temperature correlated to the localization length (ℓ_{loc}), the higher the first one, the lower the latter. The ℓ_{loc} is defined as the average spatial extension of the charge carrier wave function: the lower the T_0 , the larger the ℓ_{loc} .

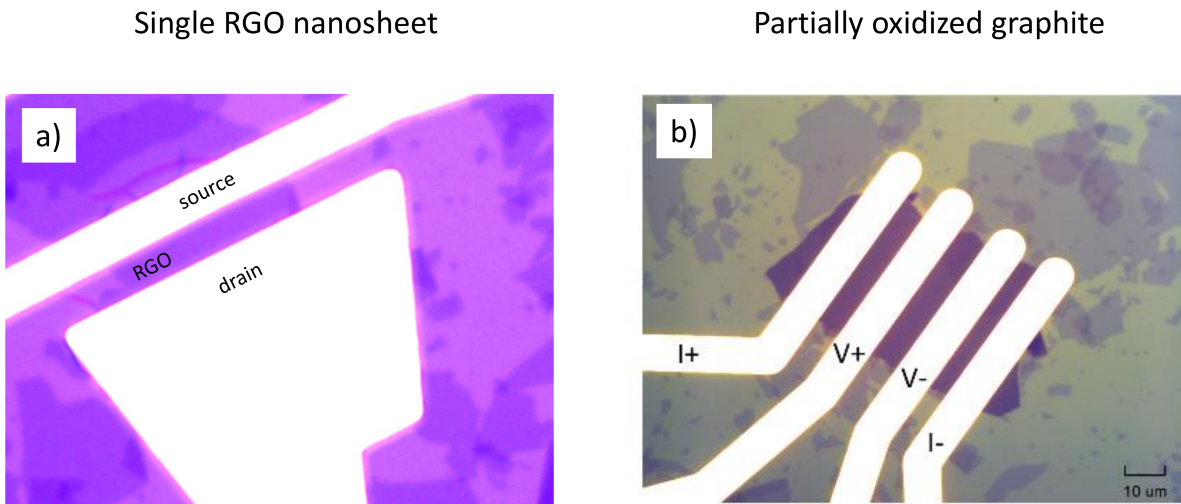


Figure S8: Optical images of devices fabricated using (a) single rGO nanosheet and (b) partially oxidized graphite. Samples thickness were measured by atomic force microscopy (AFM) and the graphitic structure of (b) was confirmed by Raman measurements.

The analytic expression reported in Eqn. S5 is quite general depending on the model commonly referred as variable range hopping (VRH). The stretching exponent β is strongly dependent on the shape of $g(E_F)$, e.g. when the density of states is constant (Mott-VRH

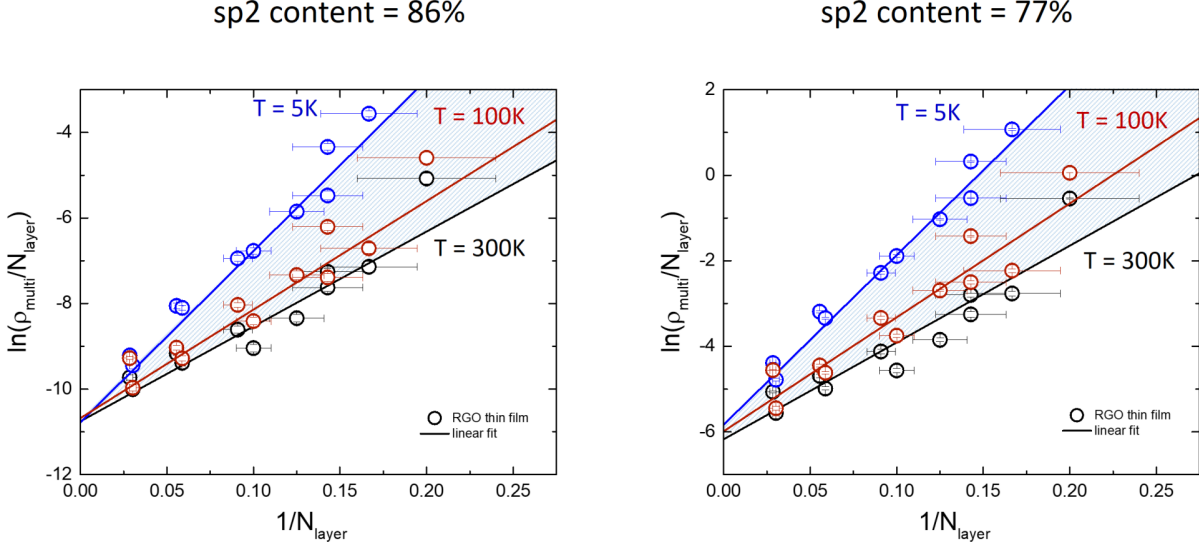


Figure S9: Correlation plots. Experimental data of multilayer RGO (circles for devices reported in Ref. 5 and acquired at different temperatures. Samples with both sp^2 contents (86% and 77%) show linear dependence, in good agreement with the theoretical prediction for scaling (cf. Eqn. 3 in the main text). All the linear fitting curves calculated at different temperatures are included between the two curves acquired at 5 K and 300 K (dashed area).

model),³¹ the β value directly depends on the system's dimension (D) with the form $\beta = 1/(D + 1)$. Reduced graphene oxide thin films show the presence of a gap at the Fermi level due to the Coulomb interaction between the occupied, excited state above E_F and the hole left by the same electron below E_F . This case is described by the so called Efros Shklovskii model (ES-VRH)³² with characteristic exponent of Eqn. S5 $\beta = 1/2$, which does not depend on the system dimensionality. The characteristic temperature T_0 for 2D materials is given by

$$T_0 = \frac{2.8e^2}{4\pi\epsilon_0\epsilon_r k_B \ell_{loc}} = \frac{1}{A\epsilon_r \ell_{loc}}, \quad (S6)$$

where e is the elementary charge, ϵ_0 and ϵ_r represent the vacuum permittivity and the relative permittivity of the material and k_B is the Boltzmann constant. For the sake of simplicity, all the universal constants are collected by the parameter $A = 0.021\mu\text{m}^{-1}\text{K}^{-1}$. Combining

Eqns. S5 and S6, we obtain the mathematical expression reported in the main text,

$$\rho(T) = \rho_0 \exp \left(\frac{1}{A\epsilon_r \ell_{\text{loc}} T} \right)^{1/2}. \quad (\text{S7})$$

Electrical resistivity measurements $\rho(T)$

Single rGO nanosheet and partially oxidized graphite were prepared by thermal annealing ($T_{\text{ann}} = 900^\circ\text{C}$) of GO and oxidized nanographite, respectively, deposited on clean SiO_2/Si substrates (2,000 rpm for 60s).

The micrometric electrodes were lithographically patterned to characterize the electrical transport across a limited number of overlapping flakes. Lithography was carried out by exposing a standard photoresist (AZ1505, Microchemicals) with the 405 nm laser of a Microtech laser writer. A 30-nm-thick Au film (without adhesion layer) was thermally evaporated onto the patterned photoresist and lift-off was carried out in warm acetone (40°C).

The resistance vs temperature measurements were carried out with a Quantum Design Physical Properties Measurements System (PPMS), using an external Keithley 2636 Source-Meter. The resistance was measured in the temperature range between 300 K to 5 K with a slow ramp (1 K/min). The Ohmic behavior of the device was checked by the linearity of the I-V curves.

Typically, each acquired $\rho(T)$ curve corresponds to an array of $>50,000$ resistivity values at different temperatures. For sake of simplicity, such $\rho(T)$ curves were sampled at 43 temperature values with logarithmic steps, as reported in Fig. S10. Three values acquired at 5 K, 100 K and 300 K are reported in Figure 5 in the main text.

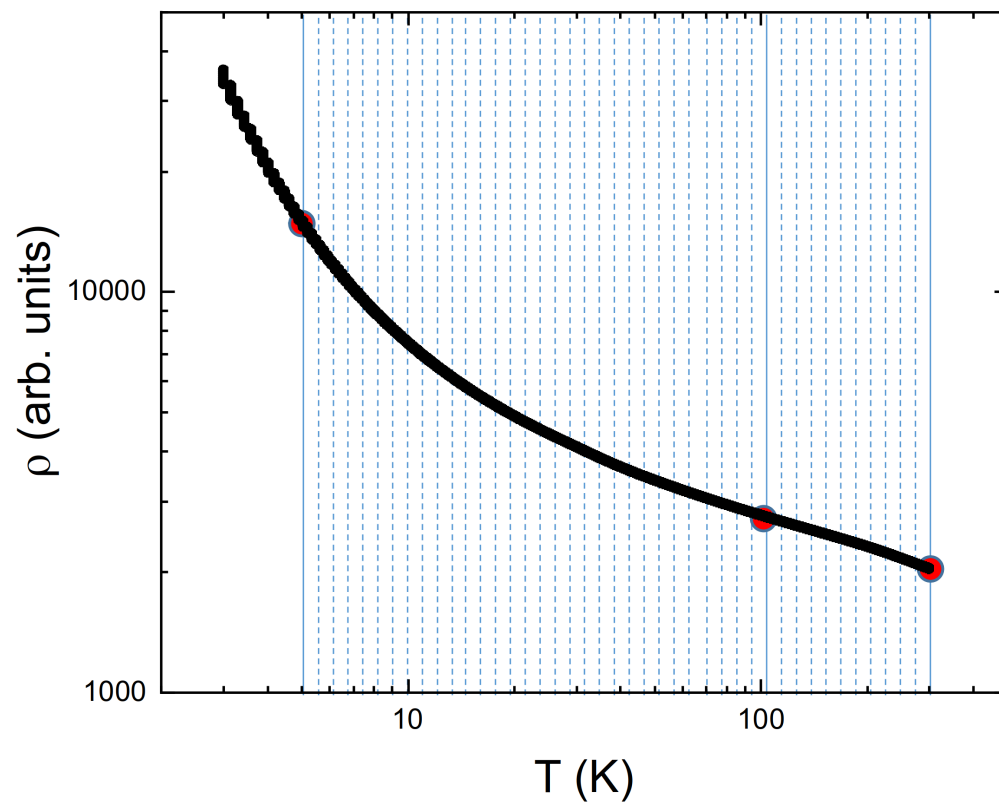


Figure S10: Example of measured $\rho(T)$ curve and sampled temperature values. Red circles correspond to the resistivity values depicted in the correlation plots.

Table 2: Summary of experimental parameters of all the studied devices

sample	N_{layer}	ξ (nm)	$\rho_{5\text{K}}$	$\rho_{100\text{K}}$	$\rho_{300\text{K}}$
single RGO nanosheet	Device 28 [ref.5 main text]	4.0±0.3			
	1	3.7±0.4			
Bi-layer RGO	Device 26	7.5±0.8			
	Device 27	7.8±1.4			
RGO thin film	Device 6	18±2	–	$(3.6 \pm 12) \times 10^{-4}$	$(2.8 \pm 0.9) \times 10^{-4}$
	Device 1	26 ± 4	$(13 \pm 3) \times 10^{-4}$	$(6.5 \pm 1.7) \times 10^{-5}$	$(4.7 \pm 1.3) \times 10^{-4}$
partially oxidized graphite		243 ± 56	$(5.9 \pm 1.3) \times 10^{-4}$	$1.1 \pm 0.3) \times 10^{-4}$	$(2.9 \pm 0.7) \times 10^{-5}$
	Device 7	7 ± 1	$(3.1 \pm 0.7) \times 10^{-4}$	$(3.4 \pm 0.8) \times 10^{-5}$	$(2.4 \pm 0.6) \times 10^{-5}$
RGO thin film	Device 17	7 ± 1	$(6.4 \pm 1.4) \times 10^{-4}$	$(1.1 \pm 0.2) \times 10^{-4}$	$(4.8 \pm 1.1) \times 10^{-4}$
	Device 2	8 ± 1	$(2.4 \pm 0.5) \times 10^{-4}$	$(3.7 \pm 0.7) \times 10^{-5}$	$(1.9 \pm 0.4) \times 10^{-5}$
	Device 8	10 ± 1	$(9.7 \pm 1.5) \times 10^{-5}$	$(1.6 \pm 0.2) \times 10^{-5}$	$(1.2 \pm 0.2) \times 10^{-5}$
	Device 3	11 ± 1	$(7.9 \pm 1.2) \times 10^{-5}$	$(2.9 \pm 0.4) \times 10^{-5}$	$(1.5 \pm 0.2) \times 10^{-5}$
	Device 9	17 ± 1	$(3.7 \pm 0.4) \times 10^{-5}$	$(1.3 \pm 0.1) \times 10^{-5}$	$(1.3 \pm 0.1) \times 10^{-5}$
	Device 4	18 ± 1	$(4.3 \pm 0.4) \times 10^{-5}$	$(1.6 \pm 0.2) \times 10^{-5}$	$(1.4 \pm 0.1) \times 10^{-5}$
	Device 10	33 ± 2	$(2.8 \pm 0.3) \times 10^{-5}$	$(1.2 \pm 0.1) \times 10^{-5}$	$(1.3 \pm 0.1) \times 10^{-5}$
	Device 5	35 ± 2	$(2.4 \pm 0.2) \times 10^{-5}$	$(2.0 \pm 0.2) \times 10^{-5}$	$(1.4 \pm 0.2) \times 10^{-5}$